Double impulse tests of long airgaps

Part 1. Engineering problems and physical processes: the basis of recent tests

Les Renardières Group

Indexing terms: *Arcing, Breakdown and gas discharges, Gas discharges, Load and voltage regulation*

Abstract: Collaborative tests have been performed using nonstandard impulses, and employing a wide range of diagnostic techniques. Part 1 of the paper describes the need for such tests, the experimental arrangement and the digital data techniques developed for the tests. Part 2 is an account of the decay of the leader channel in long airgaps and the recovery of dielectric strength. It was found that the leader conductivity had a lifetime of the order of 1 ms. In part 3 of the paper, the influence of a nonstandard impulse front on the leader growth is examined in detail. The results show that overstressing of the gap can result in a reduced probability of breakdown, and the cause of this effect is studied. In phase-to-phase structures, on the other hand, the case of a negative surge preceding a positive can be particularly dangerous: the effect of pre-existing negative space charges on positive leader growth is therefore described in part 4. Large-scale influences which cause more vigorous leader processes have been observed.

Les Renardières Group authors

A. Bertazzi, Dott. Ing., A. Pigini, Dott, Ing., Sen. Mem. I.E.E.E. and G. Rizzi, Dott., are with CESI (Centro Elettrotecnico Sperimentale Italiano), Via Rubattino 54, 20134 Milano, Italy

G. Hartmann, Dr. es Sci., is with Ecole Superieure d'Électricité, Plateau du Moulon, 91190 Gif-Sur-Yvette, France

B. Hutzler, Dr. Ing., Sen. Mem. I.E.E.E., G. Riquel and R. Diaz are with Électricité de France, B.P. No. 1, 77250 Moret sur Loing, France

R. Brambilla, Dott., is with ENEL (Ente Nazionale per l'Energia Elettrica), Bastioni di Porta Volta 10, 20121 Milano, Italy

Prof. I. Gallimberti, Dott. Ing., Prof. G. Baldo, Dott. Ing., A. Badaloni, Dott., G.-C. Pesavento, Dott. Ing., S. Stangherlin, Dott. Ing., and E. Poli, Dott. Ing., and with Istituto di Elettrotecnica e di Elettronica, Universita di Padova, Via Gradenigo 6A, 35100 Padova, Italy

G.C. Crichton, B.Sc., Ph.D., I.W. McAllister, B.Sc., Ph.D., and S. Vibholm, M.Sc., Ph.D., are with the Department of Physics, Section II, Technical University of Denmark, Building 309, DK-2800 Lyngby, Denmark

F. Rühling, Dr. Ing., is with Lehrstühl für Hochspannungs und Anglagentechnik, Technische Universität München, Arcisstrasse 21, D-8000 München 2, West Germany

P. Domens and A. Gibert, Dr. es Sci., are with Laboratoire d'Electricité, Université de Pau, Avenue de Philippon, 6400 Pau, France

A.J. Davies, B.Sc., Ph.D., C.Eng., M.I.E.E., and R. Turri, Dott. Ing., are with the Department of Physics, University College of Swansea, Singleton Park, Swansea, SA2 8PP, United Kingdom

Prof. R.T. Waters, B.Sc., Ph.D., C.Eng., F.I.E.E., A.R. Rowlands, B.Eng. (Tech), B.A., Dip. E.E., C.Eng., M.Inst.E., and A. Robledo Martinez are with the Department of Physics, Electronics and Electrical Engineering, University of Wales Institute of Science and Technology, PO Box 25, Cardiff, CF 3XE, United Kingdom

Paper 4825 (S3) received 14th January 1986

The Les Renardières Group authors are given above together with their affiliations. The tests were conducted at the Electricité de France UHV Laboratory at Les Renardières under the supervision of G. Riquel and J.-P. Riu, with participation of the staff of the laboratory and particularly M. Teigny, F. Benard, G. Faure, Y. Gossart, A. Jencewski and D. Leclaire

Valuable contributions were made by other participants during the test period and in evaluation of test results: G. Berger and A. Bondiou, Centre National de la Recherche Scientifique, R. Garabedian, Mrs Y. Jegou, Miss J. Morgan and P. Santt, Électricité de France, G. Johnson, General Electric, G. Marchesi, A. Bon, F. Celin, A. Osgualdo, G. Boccato, G. Bondani, O. Lucia and G. Flor, Istituto di Elettrotecnica e di Elettronica Padova, I. Grant, PTI, A. Huber and M. Laubenheimer, TU München, J. Dupuy and R. Peyrous, Université de Pau, W. Pfaff, E. Busse and W. Kohler, TU Stuttgart, W.T. Williams, University College of Swansea, W.B. Stark, D.M. German, J.E. Jones and M. Davies, UWIST

1 Introduction

1.1 *Nonstandard overvoltage shapes and successive surges*

The threat to the security of electricity supplies posed by overvoltages, whether these are internally or externally generated, has always been of prime importance to system designers. Engineering problems of considerable complexity arise in the estimation of the spectrum of overvoltage amplitudes and shapes which may occur, the response of the network to such overvoltages, and the consequent risk of failure of the insulation [1–6]. The resolution of these problems in a manner which is satisfactory in respect of both technical and economic limitations depends heavily on extensive testing, and this will continue to be necessary. Within the last decade, however, a great improvement in basic understanding of breakdown processes in air-insulated systems has been gained from the studies of many groups, including those of the present authors [7–10]. This is already leading towards a better appreciation of factors causing high-risk situations, a more precise quantification of insulation co-ordination specifications, and the optimisation of high-voltage test strategies [11]. This paper, which is the fifth in this series of papers prepared by the Les Renardières Group, describes results which have been obtained from physical studies in a new series of tests at the Les Renardières laboratories of Électricité de France. These physical tests have a direct practical application, as they have been designed to aid the

modelling of three types of overvoltage hazard which can occur in large air-insulated systems. All three can threaten phase-to-ground and phase-to-phase insulation and the security of system isolation. The overvoltage types to be considered are as follows:

Surge type A. Double-peak surges, where a substantial but nonsparkover discharge development from a high-voltage conductor or structure can occur during the first voltage rise; this may weaken the air insulation around that structure for the second voltage rise. Such surges have been little studied; in particular, the temporal separation which is sufficient so that two such surges can be regarded as independent is not known.

Double or multiple peak surges are known to arise in connection both with lightning and switching overvoltages. In the case of lightning overvoltages, successive peaks can be caused by inductive oscillations on the voltage front, partial chopping, travelling-wave reflections and multiple-stroke flashes. In switching operations, circuit-breaker characteristics and trapped charge effects can cause displaced peaks between phases.

In the laboratory simulation of these surges, high-frequency oscillations resembling those occurring on lightning surge fronts can be relatively easily generated, either by the use of a series inductive element giving the 1-cosine form:

$$U(t) = U_0 \exp(-at)[1 - \exp(-bt) \cos \omega t]$$

or by a double peak formed by a partial chopping on the impulse front [12]. In these ways the effect of irregular voltage application during spark growth can be studied (see the paragraph on surge type B). For impulses of switching-impulse shape with a longer time separation between peaks, however, two impulse generators are necessary, with controllable time separation of triggering. The equipment requirements and operational difficulties associated with such tests accounts for the absence of published information in this area. Part 2 of this paper is a contribution to this topic. The use of two generators also allows the tests to approximate more closely to practice in relation to phase-to-phase and longitudinal insulation (disconnectors, circuit breakers). Such insulation would in fault conditions often have the operating voltage on one side and the overvoltage on the other. Bias tests (impulse on one side, power frequency on the other) can present severe problems in terms of the requirements for large transformer capacitance (to prevent voltage distortion) and protection against breakdown. The relative severity of bias tests and the equivalent two-terminal tests (LI-SI or SI-SI) such as those used here are, therefore, of considerable technical interest [1].

Surge type B. Surges of irregular voltage rise. Spark development can be modified if the rate of rise of voltage undergoes a sharp change during the growth of ionisation in a gap. Earlier work has shown a significant effect.

Most of the available test data and physical measurements of impulse breakdown have been obtained with the simple exponential-front shapes associated with conventional impulse generators. Some early physical studies involved the application of voltage 'bumps' [13] or partial chopping [12] and examined the effect of these perturbations on breakdown probability. For engineering applications, for example, the equal-area criterion was designed to allow the effect of nonstandard impulse shapes to be ascertained from the critical condition

$$\int_0^{T_B} (U(t) - U_0)^k \, dt = K$$

where T_B is the time to breakdown, U_0 is a threshold voltage, and k and K are constants.

Although straightforward in application this seems unreliable even for double-exponential shapes because it predicts a fall in U_{50} with decreasing time to crest on the left-hand side of the U-curve [14]. More refined models involving physical quantities thus seem to be needed.

Some recent work has been reported on irregular and oscillating impulse fronts. In 4 m rod-plane gaps, Lalot and Hutzler [13] showed that a sudden application of a 'bump' voltage on a positive switching-impulse front could either increase the velocity of a propagating leader or suppress it. Consequently the probability of breakdown could be increased or decreased, depending on the time of application. Image-convertor photographs showed a reillumination of the leader when the voltage disturbance was applied. These authors also showed that the leader channel could be reignited for at least some hundreds of microseconds. In the case of partially chopped voltage fronts, it has been shown by Menemenlis that in a 3 m rod-plane gap the breakdown probability of a double-peaked front can be lower than of the second peak alone.

Some of the recent most informative measurements have employed (1-cosine) oscillating fronts [15]. In this case, the positive leader which is interrupted by the voltage troughs is reactivated by the voltage peaks. The leader velocity was found to be proportional to the rate of change of voltage as well as voltage amplitude, and semi-empirical modelling of breakdown voltage and time to breakdown under oscillating and partially chopped impulses can be made. The present tests are aimed at studying perturbations to longer discharges than those of these earlier researches.

Surge type C. Surges causing discharge growth from more than one conductor or structure in the particular case where a negative polarity discharge growth from one conductor precedes a positive voltage stress on the other. Within the last decade it has become clear that phase-to-phase switching overvoltages can represent the most severe stress conditions for air insulation. Three factors makes these conditions important in engineering terms:

(i) The magnitude of phase-to-phase overvoltages. For three-phase closing and reclosing operations, phase-to-phase overvoltages are in the range 1.4–1.8 times higher than the corresponding phase-to-earth overvoltages [1].

(ii) The α-parameter. The effect of a phase-to-phase overvoltage on air insulation for the case of synchronous opposite-polarity surges is determined not only by the total overvoltage $|U^+| + |U^-|$ but also by the relative magnitude of the two components. Thus it is found that the breakdown voltage increases approximately linearly with the value of the α-parameter, which is defined by

$$\alpha = \frac{|U^-|}{|U^+| + |U^-|}$$

Three-phase power systems in service show an α-range of 0.3–0.7. However, α-values greater than 0.5 ($U^- \geqslant U^+$) are not of direct interest because the condition $U^+ > U^-$ is always the more serious threat to the insulation.

(iii) Time-displaced phase-to-phase overvoltages. The breakdown voltage of phase-to-phase insulation can, in some cases, be reduced appreciably if the surge to the negatively stressed electrode precedes that to the positive electrode. This is, therefore, the condition defined here as surge type C. Although this effect was first shown in 1970 by Cortina *et al.* [16], who found that a breakdown voltage could arise which was 20% lower than that of the

critical flashover voltage for switching impulses, the causes of this effect are still poorly understood [17–22]. More recent studies by Zacke *et al.* [23] and Baldo *et al.* [24] have indicated that both the quantity of the negative charge created by the initial negative impulse, and its subsequent drift motion, are important in facilitating the development of the positive discharge on the later positive impulse. The aim of the present work is to obtain a greater range of data concerning this effect in a large airgap. This information is the necessary first step to allow breakdown models such as the critical-radius or leader-propagation methods [25, 26] to be adapted to nonsynchronous voltages. Secondly, it is also necessary to distinguish geometric effects (e.g. where the presence of a second negatively stressed conductor can reduce the positive switching-impulse withstand level to ground) from space-charge effects. Finally, any statistical approach to phase-to-phase safety factors [27] must take account of the statistics of time-displaced switching surges.

1.2 Physical basis

The work described in this paper is thus designed to help to model the behaviour of air insulation for surges of type A, B and C and to take account of pre-existing discharge phenomena of either polarity. Such physical tests need to be planned so as to elucidate the ways in which the characteristics of the long spark in nonuniform fields are influenced by these effects. It is useful to consider these characteristics individually and chronologically:

(*a*) The first corona development in an airgap can play a part in determining the subsequent probability of breakdown. This influence can be to increase the probability of breakdown by forming the initial phase of the leader inception process, or by traversing the gap so as to interact with the opposing structure or with ground. Conversely, the effect of corona space charge is sometimes to inhibit subsequent ionisation by space-charge quenching, so decreasing breakdown probability or at least increasing time to breakdown.

Earlier physical studies have fully established that the initiation of the first corona is frequently caused by electrons becoming available by detachment from atmospheric negative ions. Once formed, the corona streamers develop at high velocities of 1 m/μs or more, provided that a sufficiently high 'guiding field' is present in the space ahead of the streamers. The strength of the guiding field (which is the resultant of this applied field and the space-charge field) is normally about 5 kV/cm for positive streamers and 18 kV/cm for negative streamers in air at NTP [28]. It is clear that both the initiation and propagation phases of corona formation may be affected by the presence of pre-existing ionisation which can ensue from surges of type A or C. These respective effects can be studied by means of statistical time-lag data, and the charge flow and spatial development of the corona streamers.

(*b*) Pre-existing ionisation from earlier events will generally be bipolar in nature [29], with an excess of charge whose sign is the same as that of the active electrode. These ions will move by drift in the prevailing net electric field, will combine with large and small ions of the opposite sign, and will cluster with water molecules or aerosols to form large ions. In long gaps the time required to restore ambient conditions can be very long, and intervals between test impulses must lie above minimum limits. These fast and slow decay processes can be studied by electric field measurements and ion counting techniques [8, 9]. For surges of types A and B, the effect of space charge can, in some circumstances, be to reverse the direction of the electric field.

(*c*) The main phase of spark growth is the development of the leader channel. The characteristics of positive and negative leader channel propagation are now well known as a result of image-convertor studies [9, 10]. The case of a positive leader channel developing under an impulse front of critical time to crest is particularly dangerous to air insulation and is of relevance to the present tests. Here the leader grows with a 'real' velocity (taking account of tortuosity) of about 18 mm/μs between its inception and the onset of the final jump phase. In air of normal humidity (11 g/m^3) and below, the leader growth is continuous and the velocity increases only by about 40% for a doubling of the applied voltage above U_{50}. The current, however, increases from 0.6–0.8A, at U_{50}, to 5–7A, at $2U_{50}$. The tip of the leader channel forms the origin of a large leader corona in which the ionisation processes act as a current source for the leader. The tortuosity of the leader probably arises from the instability of this element of the discharge.

The effect of either sudden change in the applied voltage or the existence of a pre-ionised space ahead of the leader arising from surge types B and C is obviously important to leader growth. The present tests attempt to measure this influence on the basis of studies of leader current and velocity and associated step changes in charge flow and electric field. Spectroscopic measurements have also been undertaken.

(*d*) In humid conditions a sudden bright-up and elongation of the leader channel frequently occurs. This instability (a 'restrike') is only partly understood in terms of leader channel and leader corona conditions [9]. It is of practical importance because the probability of breakdown can be affected by this process. The influence of pre-existing leader growth, front irregularity and pre-ionization effects on restrike formation, thus need to be studied for surge types A, B and C.

(*e*) A significant improvement in the understanding of long-spark development in recent years has been based on the analysis of the hydrodynamic processes occurring in the leader channel. This has been made possible by time-resolved studies of long-spark development using schlieren (strioscopic) techniques [30, 31]. In this way, precise measurements of leader channel diameters have been achieved, which have allowed a visualisation of the shock wave and subsonic density gradients occurring at the leader tip and the leader channel 'walls'. The reduction of gas density due to gas expansion within the channel enables the ionisation processes, which are necessary to maintain leader conductivity, to proceed at relatively low electric field strength. This expansion process and increased leader conductivity provide the basic reason for the saturation of breakdown-voltage/gap-spacing characteristics and the important U-curve effect of the time to crest for switching impulses.

In the case of the objectives of the present tests for surge types A and B, the hydrodynamic properties of the leader channel are important: in the case of an irregularity in the applied voltage, the response of the leader channel cross-section will be a useful parameter. For double-peak impulses, the decay of the leader channel following the first phase may be governed as much by hydrodynamic break-up or collapse of the low-density leader as by ionic dissipation processes.

(*f*) Sparkover of an air clearance inevitably ensues (provided the voltage is maintained) when the 'final jump' is commenced. This occurs when the leader corona bridges this gap, which enables the leader current and velocity to

increase by several orders of magnitude just before the arc-through stage. Any condition which impedes or facilitates the onset of the final jump will have an influence on breakdown probability. This process has been studied during these tests for all surge types.

1.3 Organisation of the present tests

The surge types A, B and C referred to in Section 1.1 have been simulated in three laboratory experiments which were performed during October–November 1983, and which will be referred to in this paper as experiments A, B and C. All three experiments involve the use of two impulse generators, as will be described in detail in Section 2; the triggering of the generators could be displaced by a delay time Δt. The overall organisation of the experiment is indicated by the following:

Experiment	*Title*	*Electrode geometry (+/−)*	*Impulse sequence*	*Δt range*
A	Leader decay	Rod-plane	+ precedes −	400–1600 μs
B	Voltage perturbation	Rod-plane	+ precedes −	0–150 μs
C	Pre-existing space charge	Sphere-rod	− precedes +	up to 300 ms

Various impulse shapes were used, but the positive impulse time to crest of 240 μs was close to the critical flashover value. This was both to simulate the most severe engineering conditions and to evaluate the physical discharge growth as described in Section 1.2. These physical objectives also dictate the choice of electrode geometry; the gap length of 6 m represented the largest rod-plane structure with a horizontal axis which could be accommodated within the large laboratory of Les Renardières. The separately energised horizontal rod-plane arrangement of experiments A and B was a consequence of the difficulty of applying two generator outputs to the same electrode in such large systems. This arrangement did, however, also facilitate the performance of experiment C during the same test period. The choice of electrode geometry here (positive large sphere, negative rod) was governed by the requirement that no positive discharge development should occur directly as a result of the negative impulse to the rod, but that it should take place when the positive voltage was applied.

The experimental arrangement for the three experiments will thus all be described together in Section 2. As digital data acquisition was used throughout the tests, it was necessary to develop appropriate software for data analysis. Powerful data management programs have resulted from this work, which are described in Section 3. Also included in this Section are some examples of data evaluations of both electrical and optical signals.

The experimental results which have been obtained for each experiment are extensive. They are therefore presented and discussed in turn for experiments A, B and C in Parts 2, 3 and 4 of these papers. As has become the custom in this international group, the experimental data jointly obtained are presented in the main text of the paper, but interpretative discussions or additional results have been given by individual group members where appropriate in the form of Appendixes.

2 Test arrangement and measurements

2.1 Test arrangement and field computations

2.1.1 Test circuit: As indicated in the Introduction, the experiments performed during the fifth Les Renardières Group test period dealt with the behaviour of a 6 m airgap subjected to nonstandard impulses. In practice, such impulses were obtained by applying, at different instants, two double-exponential impulse voltages whose amplitude, polarity and shape could be changed as required.

For experiments A and B (i.e. leader decay and voltage perturbation, respectively) both impulses shifted by a time interval Δt could, in principle, be applied to the same electrode. For technical reasons, it was decided to apply the second impulse of reversed polarity to the other electrode, even though, in this case, the electric field distribution is not the same.

As shown in Fig. 1, a quasi-symmetrical test circuit was utilised, each branch of which involved one electrode, one damped capacitive voltage divider and one generator. The characteristics of the different high-voltage apparatuses are given in the Figure caption. Such an arrangement avoided inopportune firing of the second generator so that the time interval Δt was a fully controlled parameter.

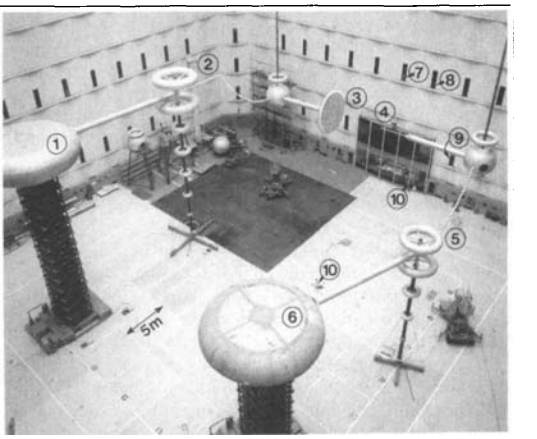

Fig. 1 *View of the test circuit with conic rod-plane gap*
1, 6: 6 MV – 450 kJ, 4 MV-300 kJ Marx generator, respectively
2, 5: 6 MV, 4 MV damped capacitive voltage divider respectively
3: ∅ 5 m plane; 4: conic rod
7: strioscopy apparatus
8, 9: image convertor cameras
10: still cameras

2.1.2 Gap and electrodes: For both the leader decay and voltage perturbation experiments A and B, the positive electrode was a 3 m long, 10 cm diameter rod terminated in a sharp cone (tip radius: 0.6 mm) in order to facilitate strioscopy measurements. The negative electrode was a 5 m diameter plane whose edges were smoothed by a 30 cm minor-radius toroid. For the pre-existing space-charge experiment C, the cone was replaced by a 25 cm diameter sphere to avoid any corona from this positive electrode during the negative discharge growth, whereas the plane was substituted as the negative electrode by a 3 m long, 10 cm diameter rod terminated by an hemisphere. These electrodes were designed to allow for charge, current and field measurements.

Table 1: Relative variation $\Delta E/E$ of the electric field at the electrodes with a progressive representation of the circuit arrangement

Configuration	Element included in field calculation	Electric field, kV/mm			
		Tip of conic rod 1 MV	Centre of plane 0 MV	Tip of conic rod 0 MV	Centre of plane 1 MV
		$\Delta E/E$	$\Delta E/E$	$\Delta E/E$	$\Delta E/E$
I	Rod-plane	296.6	0.0212	75.5	0.250
II	I + tube (rod-sphere)	266.2 −10%	0.0390 84%	72.6 −4%	0.252
III	II + spheres	256.6 −3%	0.0463 18%	79.8 +10%	0.230 −9%
IV	III + shielding toroids	247.9 −3%	0.0541 17%	100 26%	0.217 −6%
V	IV + impulse generators + leads	241.6 −2.5%	0.0609 12%	103.7 4%	0.212 2%
VI	V + laboratory walls	249.6 3%	0.0517 −15%	93.1 −10%	0.225 6%

Details of these arrangements are given in Section 2.2. In all cases, the gap length was kept constant to 6 m. The height of the horizontal gap axis was 16.8 m, and the distance with respect to the nearest wall was 17.30 m.

2.1.3 Field computations: The field computations were carried out by the charge simulation method [32]. As already reported [7, 8], the field distribution depends, not only on the shape of the electrodes and the gap length, but also on the presence of the walls, connections, dividers and generators. Table 1 shows how the field at the electrodes (conic rod-plane gap) is modified as the circuit components are successively taken into account in the simulation, until the test circuit is fully described.

All the field values considered hereafter correspond to the complete description of the test configuration. Tables 2 and 3 give the field on the gap axis at the surface of the two electrodes for the cases of conic rod-plane gap and sphere-hemispherical rod gap, respectively. For both geometries separate computations were performed to allow either electrode to be energised, the other electrode being earthed.

In most cases, the computed values have been found to be in good agreement with field measurements carried out at low voltage (to avoid modification of the field by corona).

Figs. 2 and 3 give the field distribution along the gap axis for the conical rod-plane gap and the sphere-hemispherical rod gap, respectively. Fig. 2 clearly shows the great difference in the field distribution, depending on which electrode is energised.

It should be noted that the diameter of the plane was of the same order of magnitude as the gap length. As a result, the field distribution along any diameter exhibits a minimum value close to the centre, and increases near the perimeter of the plane, as shown in Fig. 4. The discharge parameters associated with the present rod-plane configuration did not show any noticeable discrepancies compared with those obtained in more conventional test arrangements in which a large-area horizontal plane at ground level is utilised. However, in the present case the U_{50} voltage is 1555 kV ($\sigma = 98.5$ kV), instead of 1450 kV for the standard rod-plane gap.

Table 2: Computed field at the electrodes — conical rod-plane gap

	Conic rod	Centre of plane	Conic rod	Centre of plane
U, MV	1	0	0	1
E, kV/mm	249.0	0.0517	93.1	0.23

Table 3: Computed field at the electrodes — sphere-hemispherical rod gap

	Sphere	Rod hemisphere	Sphere	Rod hemisphere
U, MV	1	0	0	1
E, kV/mm	5.36	1.76	0.89	10.89

2.2 Measurements

2.2.1 Electrical measurements: The transient electrical behaviour of the discharge was studied in terms of the following:

(*a*) voltage applied to the electrodes
(*b*) electric field at the electrodes
(*c*) current or charge flowing into the electrodes.

The signals (*b*) and (*c*) were obtained from probes at the high-voltage electrodes, and the signals were transmitted to the control room by means of optical-fibre links.

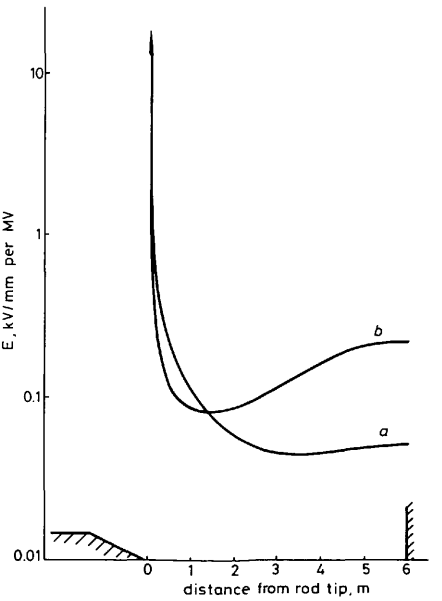

Fig. 2 *Field distribution along the gap axis for conic rod-plane gap*
a 1 MV applied to the rod, the plane being grounded
b 1 MV applied to the plane, the rod being grounded

For field measurements capacitive probes were used in most cases. Some tests, namely during experiment C (pre-existing space charge) were performed, however, with a polarised probe (field filter) at the positive electrode. All these devices have been already described in detail [10, 30]. Fig. 5 shows the location of the field probes at the different electrodes utilised during the test. Although the plane was equipped with 9 probes, the transmission device did not allow more than 3 probes to be connected simultaneously. Table 4*a* gives the main characteristics of different field measuring channels including probes, measuring capacitor and transmission device. The last line of the Table gives the ratio of the geometrical field at the probe to the field at the electrode tip. This ratio is obtained from the field computation for both potential conditions.

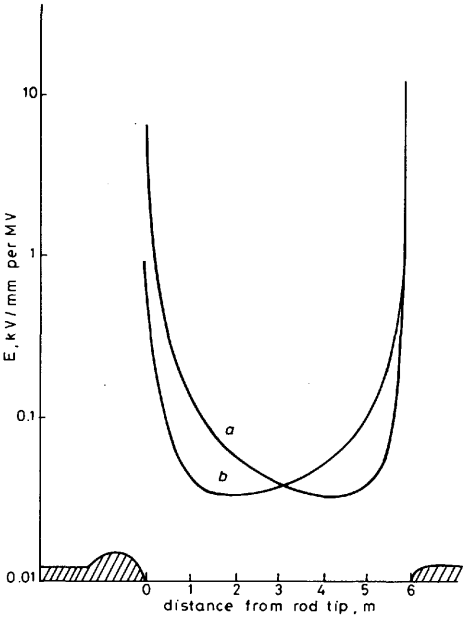

Fig. 3 *Field distribution along the gap axis for sphere-hemispheric rod gap*

a 1 MV applied to the sphere, the hemispheric rod being grounded
b 1 MV applied to the hemispheric rod, the sphere being grounded

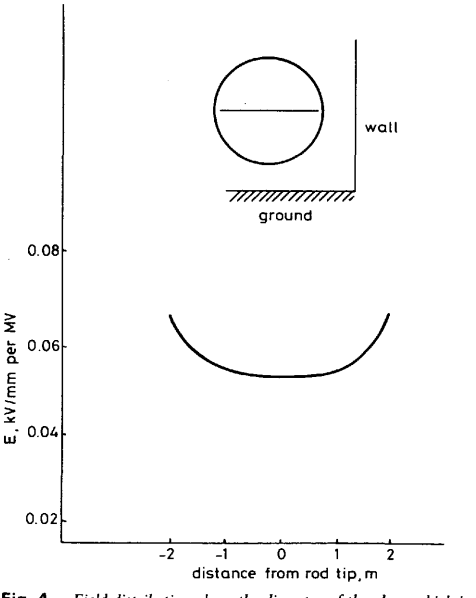

Fig. 4 *Field distribution along the diameter of the plane which is parallel to the ground, for 1 MV applied to the rod, the plane being grounded*

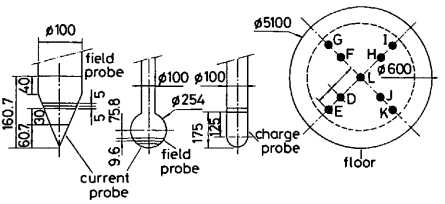

Fig. 5 *Electrodes used during the tests and location of different measuring probes*

Table 4*a*: Main characteristics of the field measuring devices

	Conic rod	ø 25 cm sphere	Plane
Bandwidth	10 MHz	10 MHz	2 MHz
Measuring capacitance	93 nF	168 nF	50 nF
Low cutoff time constant	372 ms	252 ms	500 ms
Transmission ratio	30 kV/mm.V	2.47 kV/mm.V	0.22 kV/mm.V
U, MV	1 – 0 0 – 1	1 – 0 0 – 1	
Probe/tip field ratio	0.032 0.032	0.96 0.95	

As shown in Fig. 5, the positive electrodes (conic rod or sphere) were also equipped with a current probe. These probes were connected to the main part of the electrode through a noninductive shunt of either 0.7767Ω or 2.108Ω. The current signal was transmitted to the control room with a 25 MHz bandwidth optical-fibre link whose accuracy was better than 1% [33]; see Table 4*b*.

Table 4*b*: Main characteristics of the current measuring device

Shunt	2.108Ω	0.7767 Ω
Bandwidth	25 MHz	25 MHz
Low cutoff time constant	19 ms	19 ms
Typical transmission ratio	2.6 A/V	22 A/v

$$\text{Transmission ratio} = \frac{\text{HV current, A}}{\text{Receiver output voltage, V}}$$

The charge measurements were performed at the negative rod only during experiment C (pre-existing space charge). As shown in Fig. 5 the tip of the negative electrode consisted of a 17.5 cm long capacitive probe. The charge measurement at the probe was obtained as the terminal voltage of a large value capacitor. Table 5 gives the main characteristics of the charge probe as well as the associated transmission device.

Table 5: Main characteristics of the charge measuring device

Measuring capacitor	1.98 μF
Charge on capacitor (without corona) per MV applied at the negative electrode	3.2 μC/MV
Bandwidth	2 MHz
Low cutoff time constant	≈2 s

In addition to the electrical measurements, (*a*) (*b*) (*c*) above, measurement of the electric field within the gap was made by two spherical sensors, with a fibre-optic data link, which were installed near the high-voltage electrode parallel to the axis of the gap. These sensors are designed for the measurement of two rectangular components of the electric field. They are capacitive probes consisting of a conductive hollow sphere with imbedded measuring areas on the surface. The induced charge on the measuring area is directly proportional to the electric field strength at the point of the sensor [34].

These probes showed large field changes occurring in the discharge space in both components. These could be related both to the basic discharge growth and to the reactivation and perturbation events. No detailed attempt was made during the present tests to correlate the probe signals with the spatial variations of the leader, but the test data indicate that the potential free probe can be a powerful tool for the investigation of physical processes in long-gap breakdown.

All the electrical measurements were digitised with 7612 AD Tektronix transient recorders. These each provided two independent measuring channels including an 8 bit-2 K byte recording memory. For a given transient record, the memory may be divided into several parts. Thus, a given signal may be stored and divided into domains of different sample frequency. Such a memory sharing has been useful to provide an acceptable time resolution when recording the signals for large Δt values. To increase the vertical resolution for recording of the current, both channels were utilised for the same signal. The digitisers were triggered together with either the 4 MV or the 6 MV generator. The pretrigger facility was systematically used to allow for the zero line to be easily determined.

The transient recorders were connected to HP 80 series desk computers allowing data storage on floppy disk. At the end of the tests, the data set was transferred from the floppy disks to a 9 in (22.86 cm) magnetic tape for final simultaneous analysis of all available channels for each individual impulse.

2.2.2 Optical measurements:

(i) *Photographic recordings*: The discharges were photographed by both image convertors and still cameras, suitably positioned so that time-resolved 3-dimensional pictures of the discharge could be reconstructed. As in all the experiments two different impulse voltages were applied, it was necessary to record two different phenomena shifted in time. In order to have a good time resolution in both cases, two photographic systems were used, each with an image convertor camera synchronised, respectively, with the firing of the first and second impulse generators. The position of the horizontal axis of the gap, which was 16.68 m above ground, did not allow the best choice of recording system locations. In particular, the image convertors observing the two phenomena, and also the still cameras, were far from one another. The picture evaluation and the comparison of the two sequential phenomena became quite complex; this has been achieved by using image digitisers and computer facilities.

(ii) *Spectroscopic analysis*: During the voltage perturbation tests of experiment B, one fixed experimental condition was chosen and a time-resolved spectrum from 250 nm to 780 nm was investigated. The measuring set-up, which was located 5 m above ground and 19 m from the gap axis, is schematically presented in Fig. 6. A rectangular region 8 cm from the tip of the rod, and of dimensions 15.7 mm × 450 mm, was selected for these spectral observations.

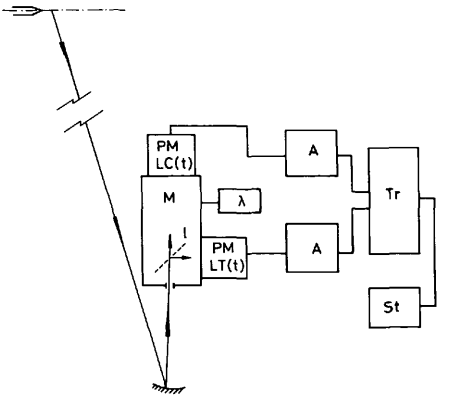

Fig. 6 *Sketch of the spectroscopy apparatus*
M = monochromator
λ = remote control of the wavelength
I = quartz beam splitter
P, M = photomultipliers for *LC* and *LT*, respectively
A = transient recorders
Tr = computer
St = data storage

The Jobin and Yvon monochromator type H 20 UV, 200 mm focal length and *f*/3.5 aperture was equipped with a holographic grating of 1200 grooves/mm. Its spectral bandwidth ranged from 200 to 800 nm with a maximum efficiency at about 370 nm. Both chromatic light (*LC*) and total light (*LT*) were recorded simultaneously through two photomultipliers HAMAMATSU R 928. By using a quartz beam splitter placed just behind the input slit of the monochromator oriented at 45° with respect to the optical axis, the observed region was systematically the same for both signals, allowing for an excellent normalisation of the *LC* signal by the *LT* signal.

The $LC(t)$ and $LT(t)$ signals were digitised by using two 7 912 AD Tektronix transient recorders. For each voltage application all information, namely the $LC(t)$ and $LT(t)$ signals, the wavelength and the vertical sensitivity of the digitisers, was stored on tape. For all impulses, the current signal measured at the positive electrode was also recorded.

(iii) *Strioscopic measurements*: Strioscopic measurements were performed during all the tests to visualise the leader channel expansion. The experimental arrangement is presented in Fig. 6. Owing to the characteristics of the device, the observed zone of the gap was approximately 5 cm, so that a conical electrode had to be chosen to ensure that the leader was in the field of view. Compared with other experiments, large difficulties in adjustment had to be overcome due to the fact that the two mirrors (M1 and M2 in Fig. 7) were placed 70 m apart at a height of 16 m above ground. The light duration of the auxiliary luminous source imposed the limit that different discharge phases delayed more than 300 μs could not be observed during the same voltage application.

The image convertor camera which was used to obtain strioscopy results was used in two different modes (Fig. 8). In the framing mode, the schlieren records of the leader channel which allow the determination of its thermal diameter were recorded at successive instants. It was found generally more effective to use the streak mode, where the continuous temporal evolution of a section of the channel

could be recorded for a long period. This gave a direct measurement of the development of the thermal diameter as a function of time.

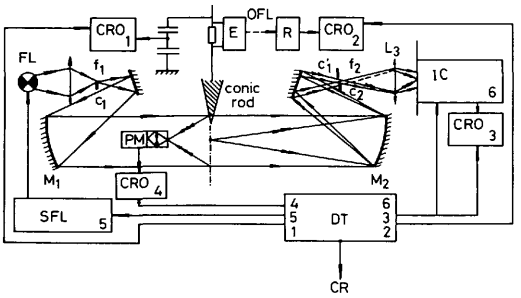

Fig. 7 *Sketch of the strioscopy apparatus*
CRO: Oscilloscopes
E, R: emitter and receiver of the optical fibre link
FL-SFL: Flash Lamp and its supply
IC: Image convertor
PM: Photo multiplier
D, T: Delay and trigger
CR: Control room

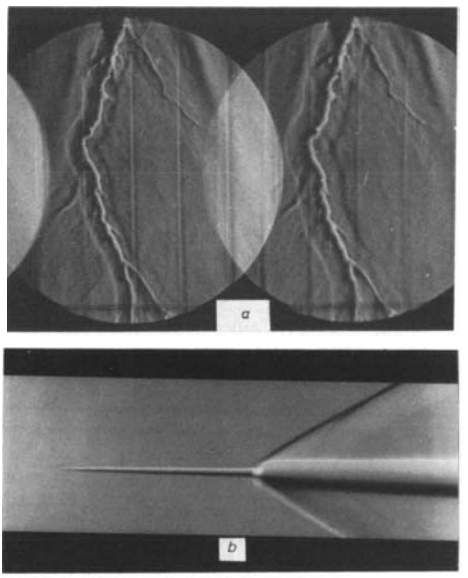

Fig. 8 *Thermal images of the leader channel*
a Frame mode
b Streak mode

3 Integrated software for data evaluation

3.1 General description

The simultaneous recording of many electrical signals, together with static, streak and strioscopic photographs, and the amount of information collected during the whole test period raised the necessity of preparing adequate software packages to store the data, to visualise them, to correlate the electrical signals to each other and with the photographic recordings, and to analyse statistically the results of evaluation.

During the experiments two basic types of data have been collected: the electrical signals, sampled by the acquisition digitisers and recorded on a magnetic support; and the photographic records, obtained mainly as Polaroid pictures. These two types of data have been analysed according to different numerical procedures and then correlated to each other. The flow chart of the integrated procedures which have been realised is represented in Fig. 9.

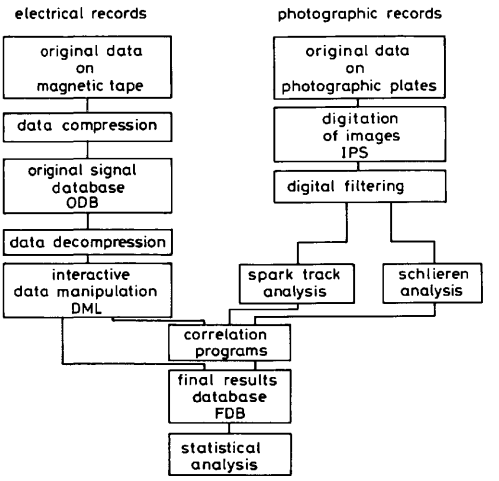

Fig. 9 *Structure of the integrated software packages for data evaluation*

The electrical signals have been organised into the structured 'original database' (ODB) from which it was possible to sort any signal on any desired timescale. Before storage into the ODB, the signals were compressed to reduce the total space used on the mass-storage device; decompression routines were then used when sorting the signals from the ODB.

The sorted signals were then passed to the DML program† (data management language), which is an interactive vectorial calculator, able to produce a large number of evaluations and correlations on the different signals. The quantitative results of the evaluations (current peaks, total charge, field changes etc.) could then be stored into a relational 'final database' (FDB), where they could be accessed by the routines performing, for example, the statistical analysis of the evaluated results.

The photographic results have been analysed by an 'image processing system' (IPS). The IPS consists of a video camera which digitises the image directly into a 512 x 512 matrix of RAM memory (8-bit intensity scale). Here the image can be passed through digital filters (in order to clean the noise, to enhance the contrast, to sharpen the edges etc.). No database of the digitised images has been created, because the space on the mass storage device would be too large; and the original photographic plates could be redigitised by the IPS directly in the RAM memory, in a time shorter than that necessary to sort them from any database.

The digitised images are then used to analyse the 3-dimensional and temporal evolution of the spark track, or to evaluate the time changes of the leader cross-section. The results obtained are then passed to 'correlation programs', to be compared with the DML signals. The quantitative values of the final results are then stored in the FDB, for the statistical evaluation, together with all the other final results.

† This software has been developed at Padova University by G. Boccato, G. Bondani, F. Celin, I. Gallimberti, O. Lucia and S. Stangherlin.

The interface between the different software modules can be direct, in the sense that they are organised into a sequential routine which activates the different modules in cascade, or indirect in the sense that all the information evaluated by a software module is stored into a standardised 'metafile', where it can be accessed by any other software modules.

In the following subsections the different modules reported in Fig. 9, are briefly described.

3.2 Original signals database

The signals sampled during an individual test shot (6–12 electrical channels) were recorded into a single file and then distributed altogether on magnetic tapes. Each channel consists of a vector of 2048 integers, plus a 400 bytes string where the identification code is written, together with all the scaling factors (vertical amplification, zero-line offset, sampling times, triggering delay etc.).

The original signal database (ODB) has been organised as a 'structured' file database: the total allocated space has been divided hierarchically into 'series' and 'subseries': the series correspond to test periods with unchanged electrode configuration and voltage waveshapes; the subseries correspond to test periods within a series under identical conditions (with unchanged voltage levels and firing delay between the two Marx generators).

The files of individual shots have been therefore inserted into the ODB with a series and a subseries identification, so to group them for identical experimental conditions. Before insertion into the ODB each file was compressed, while a decompression routine was used when sorting it from the ODB.

A special compression algorithm has been designed for this application. The 400 byte string was simply reduced to the minimum formatted space for shot identification code and integer or real scale factors; the 2048 vector of integers (16 bit each) has been compressed according to a 4-way algorithm based on the difference between subsequent sample points (Fig. 10). In a regular sampled signal the difference Δ between subsequent sample values is generally small: in many cases, it can even be zero for quite a large number of samples.

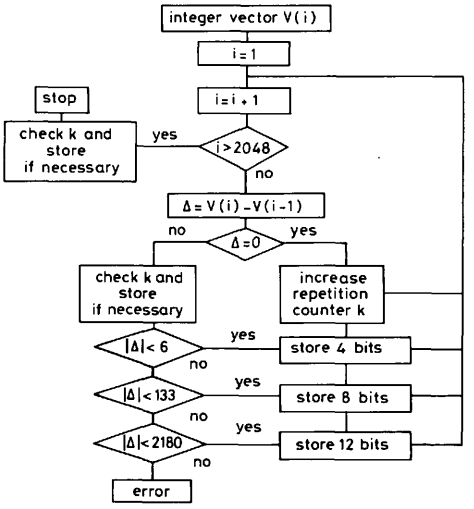

Fig. 10 *Algorithm for signal compression*

If the absolute value of Δ is $\leqslant 6$, then it can be stored into a 4 bit elementary module (Fig. 10), or else it has to be stored in longer elementary modules (8 bits for $|\Delta| \leqslant 133$ and 12 bits for $|\Delta| \leqslant 2180$). As the 4 bit elementary module represents 16 combinations, three of them are in excess with respect to those necessary to store $|\Delta| \leqslant 6$; hence, two of them can be used as control codes (CC) to introduce 8 bit or 12 bit elementary modules. The compression efficiency is therefore respectively 75%, 25% and 0%.

The compression efficiency can be further improved, if the last available 4 bit control code is used to introduce the repetition case: when $\Delta = 0$ appears more than twice, a counter is activated and stored, after the end of the equal sample sequence, preceded by the adequate control code).

The decompression algorithm operates exactly in the same way (Fig. 10), but in the 'read' mode instead of the 'write' mode.

The practical compression efficiency obtained for the ODB was around 80% with an improvement by a factor of 5 in the space allocated in the mass storage device; Table 6 gives some details of a statistical analysis on the occurrence of the possible '4-ways' of the compression algorithm.

Table 6: Statistical analysis of the compression algorithm in the case of the ODB signals

Way number	Occurrence frequency	Compression efficiency
(1) $\|\Delta\| \leqslant 6$	79.04%	75%
(2) $6 < \|\Delta\| \leqslant 133$	9.52%	25%
(3) $133 < \|\Delta\| \leqslant 2180$	0.02%	0%
(4) Repetition	11.42%	92%

3.3 Interactive data manipulation

The DML program has been developed starting from the basic idea that any group of signals, when sorted from the ODB on the same timebase (initial time, sampling interval and number of points), is simply a group of vectors which can be manipulated with any possible algebraic combination or analytical transformation. A 'vectorial calculator' has been therefore developed, based on the use of 'stack registers' and RPN, like the usual HP pocket calculators. By introducing commands from the keyboard it is possible to execute operations on the memory registers of the calculator.

The stack has four registers (X, Y, Z, T) each of 2048 real numbers: the X register can be loaded from the keyboard, from the ODB, or from specific files on the mass storage. The stack can be moved up or down with the commands 'enter' and 'roll'; it is automatically moved up when entering a new X value. Operations with a single argument (like $1/X$, $\sqrt{X}$, sin (X) etc) are executed directly on the content of the X register, in succession for all the 2048 vector components; the X content is saved in the additional register $LASTX$. Operations with two arguments are executed on the registers X and Y, in succession for all the 2048 vector components, and the result is stored in X.

Some additional storage registers, numbered starting from 0, are available for temporary storage of intermediate results, which can be recalled in the X register at any time.

Some additional functions, typical of signal processing, have been added to the basic vectorial calculator:

(*a*) *Timescale commands*: to fix the individual or common time bases, and to synchronise signals in different registers.

(*b*) *ODB access commands*: to sort signals from the ODB, in the desired timebase (interpolation is used when this timebase does not coincide with the sampling times), and on the correct vertical scale.

(*c*) *Graphic facilities*: to plot the content of one or more stack registers on graphic terminals, to hard-copy them on graphic printers or plotters, to zoom portions of the display etc.

(*d*) *Integration and differentiation*: commands have been implemented to perform definite or indefinite integration and differentiation of the signal in the X register.

(*e*) *Digital filtering*: a number of digital filters (essentially low-pass) with different bandwidth characteristics have been implemented to clean noisy signals when needed.

(*f*) *Identification*: of peaks, steps and smooth scroll analysis of signal fine details.

(*g*) *Fast fourier transform*: to study the frequency characteristics of signals and their eventual correlation properties.

The DML program is composed of two essentially distinct sections (see Fig. 11): the first one is the 'command interpreter', the second one is the 'command executor'. The command interpreter has been designed to accept a single command, a command line or a command file: this latter possibility makes the vectorial calculator programmable, which can be very useful in the case of systematic repetitive evaluations. Command files can be activated also during the execution of other command files up to a maximum nesting level of 4, introducing in the programmability of the vectorial calculator also the command subroutines.

Each of the accepted commands is composed of its name followed by one or more eventual parameters; the latter may be integer (like the specification of a storage register) or real (like the definition of a zoom region). The command interpreter scans each command line (introduced by the keyboard or by command file), separates the command names from the respective parameters and prepares the following vectorial stacks for the command executor:

(i) *Command stack*: contains the sequence of commands, coded in an adequate integer form; a pointer can scan the command stack and cause them to be executed in sequence

(ii) *Integer parameter stack*: contains all the integer parameters entered with the commands; a pointer is moved along this stack under the control of the command stack pointer

(iii) *Real parameter stack*: contains all the real parameters entered with the commands; also here a pointer is moved under the control of the command stack pointer.

These three stacks contain all the information of the command line, in a form adequate for the command executor to call the execution routines and to pass them the necessary parameters (see Fig. 11).

An example of a work session with the DML program is given in Fig. 12, where the command sequence and the

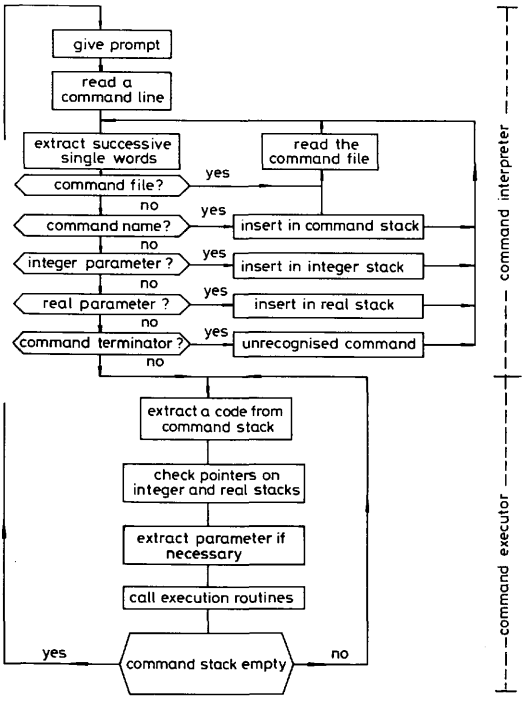

Fig. 11 *Structure of the DML main program*

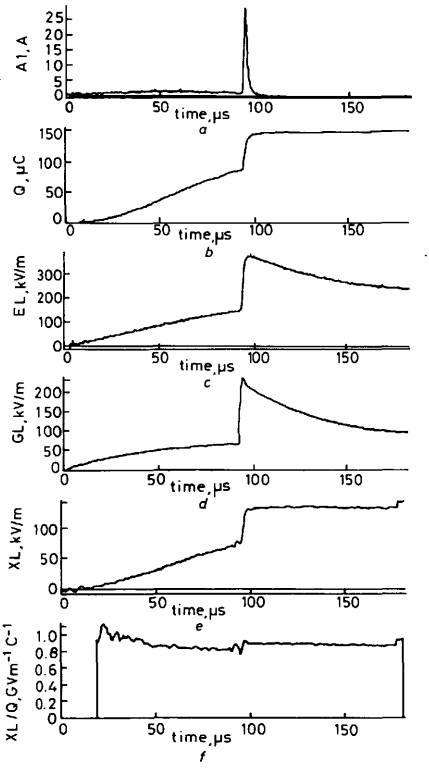


```
DML> TBASE 0. 182.E-6 2048
DML> DL 0 TT 6
DML> SERIES 8.4
DML> SHOT 771848
DML> GET A1 PLOT
DML> INTEGRATE PLOT
DML> STORE 1
DML> GET EL PLOT
DML> STORE 2
DML> GET V+
DML> 0.519 x
DML> GET V-
DML> 2.143 x CHS + PLOT
DML> RECALL 2 X><Y -
DML> PLOT
DML> FILTER 10 0. 182.E-6
DML> SHIFT -0.5E-6
DML> RECALL 1 /
DML> PLOT
```

Fig. 12 *Illustration of a DML work session*

hard-copies of the video-terminal plots are reported. The example illustrates how it is possible to derive the ratio of the space-charge field to the charge, starting from the measured current, voltage and field oscillograms.

First the desired series, subseries and shot number are selected, together with a common timebase for all the signals; then the current signal I is sorted from the ODB and integrated to obtain the charge Q: the latter is stored in register 1. Then the field EL is sorted and stored in register 2. To obtain the pure space charge field XL it is necessary to subtract from EL the geometric field GL produced by both the positive U^+ and negative U^- voltages applied, respectively, to the point and plane electrodes. To obtain the voltage it is enough to use the calculated field constants reported in Table 2 and add the contributions of U^+ and U^-. With the zoom command, the synchronisation of EL and GL at the instant at which U^- is applied can be easily checked: if a timeshift appears (due to jitter in the triggering circuits), this can be corrected with the shift command to obtain a correct alignment. Then GL can be subtracted from EL to obtain the space-charge field XL. As XL derives from a difference, the random noise is particularly high, so that it may be useful to filter it: in the example of Fig. 12*e* a low-pass filter with a bandwidth 10% of the sampling frequency has been used.

The charge Q is then recalled from register 1, and after the check of the sycnhronization with the XL signal, the ratio XL/Q can be obtained: this gives an indication of the position that the discharge space charge occupies within the gap.

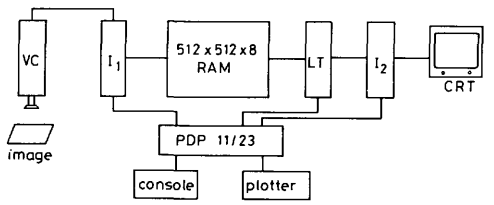

Fig. 13 *Schematic representation of the image processing system*

3.4 The image processing system and programs

The structure of the image processing system is represented in Fig. 13. The image is scanned by the video camera (VC). The interface I_1, under the control of a PDP 11/23 processor, makes it possible to digitise the image and to load it in a RAM matrix of 512 × 512 pixels with an intensity scale of 8 bits per pixel. This RAM memory can be directly accessed by the processor via the computer bus. The digitised image can then be displayed on a colour screen, via the interface I_2 also under the control of the PDP 11 processor, after having been passed through the lookup table (LT): this fixes the characteristics of visualisation of the 8 bit intensity scale (linear or nonlinear grey

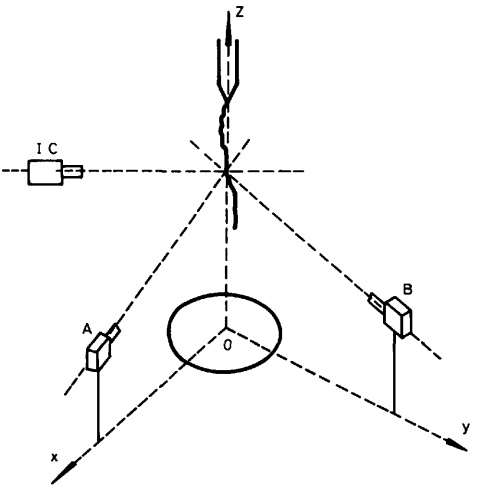

Fig. 15 *Schematic representation of the photographic arrangement for leader track analysis*

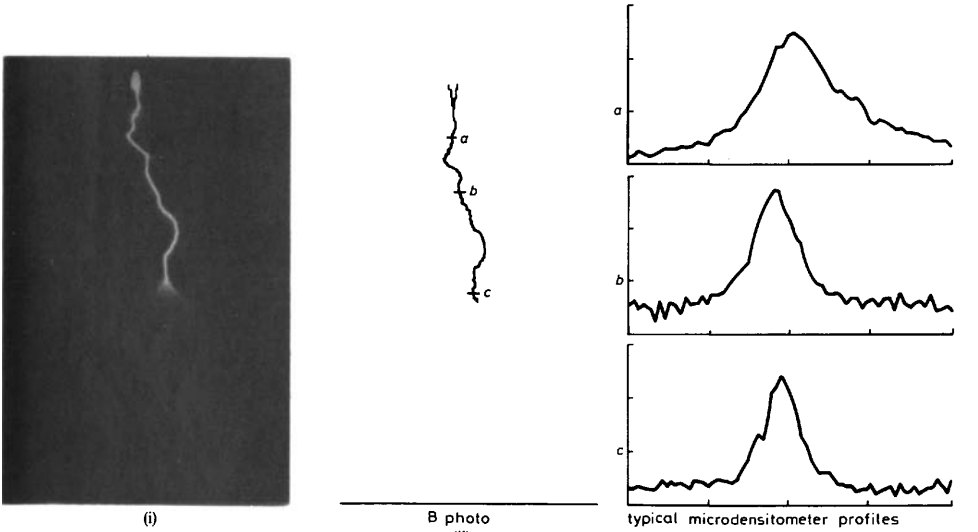

Fig. 14 *Example of intensity profiles*

(i) Leader channel still photograph; (ii) Leader track digitised with the pattern recognition routines; (iii) Cross-section intensity profiles in three different positions

scales, artificial colour scales, number of colours etc.). The lookup table can be programmed by the operator, selecting the type of intensity visualisation which best reveals the desired details in the image. In addition, the image can be manipulated by the processor: digital filtering routines have been implemented to clean random noise, to enhance the contrast, to sharpen the edges etc.

Some general purpose routines have been implemented for analysis of discharge photographs, essentially for pattern recognition and for tracing intensity profiles.

The pattern recognition routine gives the co-ordinates of a number of points along the discharge track in the photograph reference frame. A light pen is used to introduce the basic points of the reference frame. The algorithm can be fully or partly automatic: in the first case, the initial point of the track is assigned with the light pen and the algorithm moves along the track by searching a 'relevant' point (maximum or minimum intensity, maximum intensity derivative etc.) along an half circle of fixed radius centred in the last point. This algorithm may fall into ambiguity in the case of discharge branching. The partly automatic algorithm avoids these ambiguities, because a 'preferential track' is assigned with the light pen, in a very approximate way: the algorithm then searches for the 'relevant' points along lines orthogonal to the 'preferential track', starting from the preferential track itself.

The routine for tracing intensity profiles can display and store the intensity distribution along a straight segment across any portion of the digitised image. The extreme points of the segment are fixed by the light pen; the segment across the image is then visualised and the intensity profile is automatically displayed (in a linear grey scale).

An example of the results of these general purpose routines is given in Fig. 14, where the still photograph of a leader channel is reported, together with its digitised track

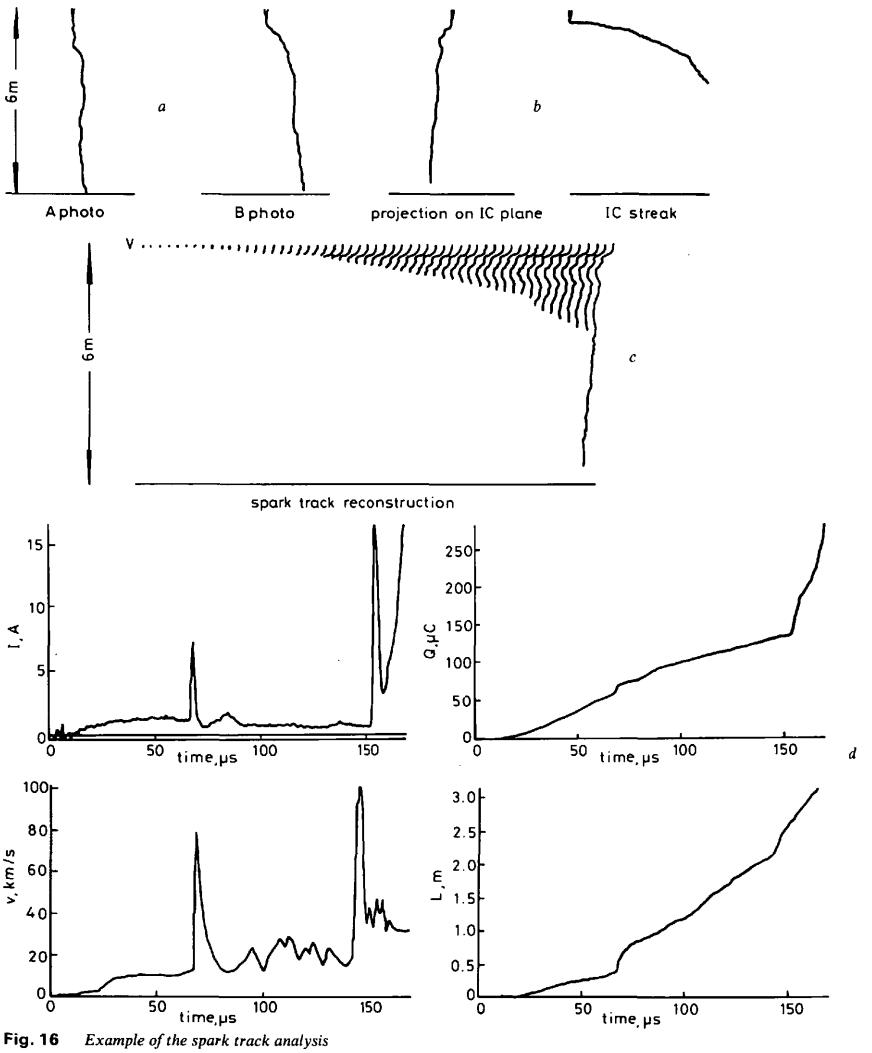

Fig. 16 *Example of the spark track analysis*

a Static photographs
b Still projection and IC streak
c Simulated framing sequence ($\Delta t = 10$ μs)
d Real velocity and length against time compared with current and charge

and with the cross-section intensity profiles at different longitudinal positions.

Two groups of evaluation programs have been then prepared for the analysis of the digitised photographic recordings collected during the test period.

The first group deals with the 3-dimensional and temporal reconstruction of the leader track, starting from two digitised static pictures taken at almost perpendicular directions (Fig. 15), and one or more digitised image convertor streaks. The principle of the method is very simple: as the projections of the filamentary leader channel on the planes perpendicular to the optical axis of the static cameras are known (Fig. 16*a*), simple relations of projective geometry make it possible to build up its 3-dimensional track. The latter is then projected on the plane of the image convertor and compared with the image convertor streak (Fig. 16*b*), to separate the spatial deviation from the timeshift.

In this way, the time at which the leader head has passed any point of the three-dimensional track can be determined. A discharge framing sequence projected on any observation plane can then be obtained (Fig. 16*c*), together with length/time or velocity/time plots, to be correlated with the electrical signals evaluated with the DML program (Figs. 16*d* and *e*).

The second group of evaluation programs deals with the analysis of the neutral density distribution across a section of the leader channel, starting from the strioscopic frame or streak recordings.

Such a picture presents always a grey background, which represents the gas where no perturbation of the refractive index is present; on this background brighter or darker regions appear depending on positive or negative light deflection from a 'gas body' where the refractive index is modified. Under ideal conditions the intensity change is proportional to the deflection angle, which in turn is proportional to the gas density gradient. Therefore, for a plane 'body', perpendicular to the light direction, the integration of an intensity profile would give the profile of gas density variations. For a cylindrical 'body', as we can assume the leader channel to be, the simple integration has to be replaced by an inverse Abel transformation; however, in most cases, the simple integration also gives qualitative information on the gas density distribution, with a much shorter computation time.

Both procedures have been implemented: the digitised frame or streak photographs are first cleaned of random noise to obtain an uniform grey background (Fig. 17*a*). Then the intensity profiles, at a given section, are plotted at different successive times (Fig. 17*b*). If necessary, routines for smoothing and for correcting nonuniform illumination can be used, before integration or Abel-inversion.

The obtained radial density profiles (Fig. 17*c*) give information on the neutral density evolution in the leader channel, following the energy input associated with the charge flow.

3.5 Final results database

The results of the quantitative evaluation of both electrical signals and photographic recordings of a single shot are a number of quantitative parameters (e.g. charge, current electric field, leader length and velocity, at given relevant times or at the end of the propagation), which have to be stored and then statistically compared with analogous results for other shots under similar or modified experimental conditions.

For this purpose a relational database has been

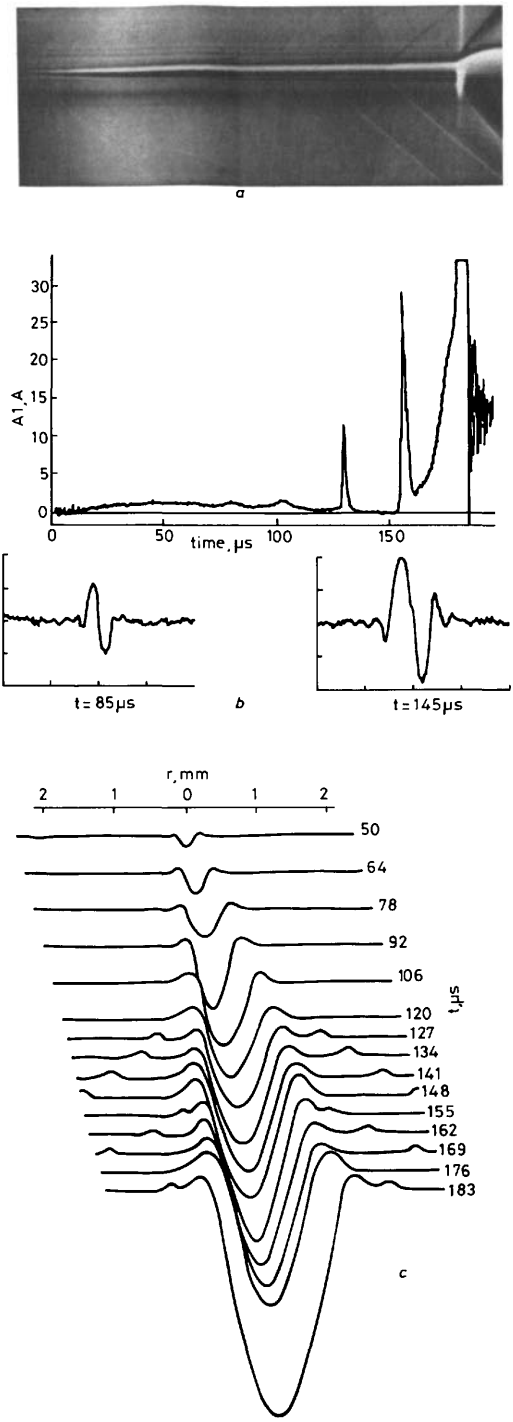

Fig. 17 *Example of analysis of a strioscopic streak record*
a Initial photograph of the leader expansion
b Intensity profiles across the leader section at successive times
c Relative density variation across the leader section against time

designed (FDB), based on the Hydra System developed a few years ago at CERN.

All the memory space allocated for the FDB is in a single vector called dynamic storage. The elementary cell within the dynamic storage is the bank; it is identified by the address of its status word and contains two distinct memory sections: the data area which can contain any real or integer number or any character string, and the Link area which contains pointers to other banks. Through these pointers a relational structure within the database can be built up; and it is possible to move from bank to bank following a relational procedure.

The structure of the FDB (Fig. 18) has been organised vertically along the tree 'series-subseries-shots-channels', and horizontally into chains of similar banks. This makes

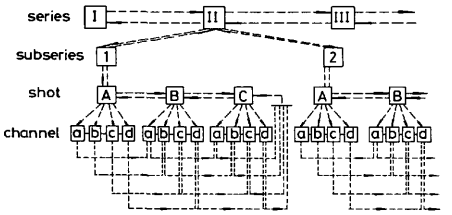

Fig. 18 *Relational structure of the final result database*

possible any type of systematic search for parameters, or group of parameters, at any level of homogeneity of experimental conditions (shot, subseries, series) and the use of interactive programs for statistical analysis, regression and data best-fit.

4 Conclusion

This paper describes several types of surges which lead to special engineering hazards in, for example, phase-to-phase insulations. A programme of tests was defined to investigate the properties of air insulation for voltage stresses of this kind. The organisation of the tests was planned to examine the influence of such surges, particularly on leader properties.

Practical techniques have been developed in both the high-voltage technology to realise these tests and in the digital acquisition and processing of large quantities of electrical and optical test data. These have been made sufficiently general to be applicable to a very large variety of gas discharge and plasma physics experiments.

The detailed conclusions concerning the behaviour of air insulation under double-impulse voltages will be described in the following papers: Parts 2, 3 and 4.

5 Acknowledgments

The authors wish to thank EdF for the use of the Les Renardières UHV Laboratory and the invaluable support of its staff.

The authors are also indebted to the following organisations for financial support: CNR (Centro Nazionale di Ricerca), Italy, CNRS (Centre Nationale de la Recherche Scientifique), France, Danish Natural Science Research Council, Denmark, Danish Technical Research Council, Denmark, DFG (Deutsche Forschungsgemeinschaft), Germany, ENEL (Ente Nazionale per L'energia Elettrica), Italy, and SERC (Science and Engineering Research Council), UK.

6 References

1 WECK, K.-H.: 'Principles and procedures of insulation co-ordination'. Presented at IEE Conference on Lightning and Power Systems, Savoy Place, London, 5th–7th June 1984 (to be published, *IEE Proc. C, Gen. Trans. & Distrib.*, 1987, **134**)
2 CARRARA, G., and YAKOV, S.: 'Statistical evaluation of dielectric test methods', *Energia Elettrica*, 1983, (1), pp. 12–19
3 MENEMENLIS, C.: 'Statistical estimation of phase-to-phase risk of failure', *IEEE Trans.*, 1981, **PAS-100**, pp. 812–821
4 CIGRÉ STUDY COMMITTEE 33: 'Switching impulse strength of phase-to-phase external insulation', *Electra*, 1979, (64), pp. 158–181
5 CIGRÉ STUDY COMMITTEE 33: 'Design and testing of phase-to-phase insulations', *ibid.*, 1979, (64), pp. 184–210
6 CIGRÉ STUDY COMMITTEE 33: 'The influence of non-standard conditions on the switching impulse strength of phase-to-phase insulation', *ibid.*, 1979, (64), pp. 211–230
7 LES RENARDIÈRES GROUP: 'Research on long air gap discharges at Les Renardières', *ibid.*, 1972, (23), pp. 53–157
8 LES RENARDIÈRES GROUP: 'Long air gap discharges at Les Renardières: 1973 results', *ibid.*, 1974, (35), pp. 49–156
9 LES RENARDIÈRES GROUP: 'Positive discharges in long air gaps at Les Renardières', *ibid.*, 1977, (53), pp. 31–153
10 LES RENARDIÈRES GROUP: 'Negative discharges in long air gaps at Les Renardières', *ibid.*, 1981, (74), pp. 67–216
11 JONES, B., and WATERS, R.T.: 'Air insulation at large spacings', *Proc. IEE*, 1978, **125**, pp. 1152–1176
12 MENEMENLIS, C., and HARBEC, G.: 'Behaviour of air insulating gaps stressed by switching overvoltages with a double peak', *IEEE Trans.*, 1978, **PAS-97**, pp. 2375–2381
13 LALOT, G., and HUTZLER, B.: 'Influence of non-standard SI on the flashover mechanisms of an air gap', *IEE Trans.*, 1978, **PAS-97**, pp. 848–856
14 HUTZLER, B.: 'Space charges in large air gaps', *ISH (Athens)*, 1983, paper 42.02
15 BALDO, G., and PESAVENTO, G.C.: 'Leader propagation under lightning overvoltages with different gap lengths', *ibid.*, 1983, paper 42.05
16 CORTINA, R., SFORZINI, M., and TASCHINI, A.: 'Strength characteristics of air gaps subjected to interphase switching surges', *IEEE Trans.*, 1970, **PAS-89**, pp. 448–452
17 ALEKSANDROV, G.N.: 'A study of the electric strength of phase-to-phase air gaps in compact overhead lines', *ISH (Athens)*, 1983, paper 44.11
18 WECK, K.-H. *et al.*: 'Phase-to-phase and longitudinal insulation technique'. CIGRÉ, paper 33-09, 1976
19 CARRARA, G., PIGINI, A., and POLO-DIMEL, M.: 'UHV disconnectors: switching surge design and testing of external insulation', *IEEE Trans.*, 1978, **PAS-97**, pp. 2094–2103
20 KISHIZIMA, I. *et al.*: 'New facilities for phase-to-phase switching impulse tests and some test results', *IEEE Trans.*, 1984, **PAS-103**, pp. 1211–1216
21 GRANT, I.S., and PAULSON, A.S.: 'Phase-to-phase switching surge design'. Report EPRI-EL-3147, 1983
22 KOSZTALUK, R. *et al.*: 'Effect of time shift between the two voltage components on phase-to-phase insulation strength', *IEEE Trans.*, 1981, **PAS-100**, pp. 3379–3386
23 ZACKE, P., FISCHER, A., and BOECKER, H.: 'Breakdown phenomena of rod-rod gaps under impulse voltages of opposite polarity on both electrodes *IEEE Trans.*, 1977, **PAS-96**, 701–708
24 BALDO, G. *et al.*: 'Phase-to-phase insulation: effect of time shift between the two components of the applied voltage', *ISH (Milan)*, 1979, paper 52.18
25 CARRARA, G., and THIONE, L.: 'Switching surge strength of large air gaps: a physical approach', *IEEE Trans.*, 1976, **PAS-95**, pp. 512–520
26 HUTZLER, B., and HUTZLER-BARRE, D.: 'Leader propagation model for predetermination of switching surge flashover voltage of large air gaps', *IEEE Trans.*, 1978, **PAS-97**, pp. 1087–1096
27 'Insulation coordination, Part 3: Phase-to-phase insulation coordination. Principles, rules and application guide'. IEC Publication 71–3, 1982
28 WATERS, R.T. *et al.*: 'The structure of the impulse corona in a rod/plane gap. II. The negative corona', *Proc. Roy. Soc. A*, 1979, **367**, pp. 321–342
29 ALLEN, N.L., CLARK, P., DRING, D., and WATERS, R.T.: 'Ionic combination and the estimation of the negative-ion component in positive corona'. *Int. Conf. Gas Discharges & Appl.*, Oxford, 1985, pp. 163–166
30 WATERS, R.T.: 'Diagnostic techniques for discharges and plasmas', *in* KUNHARDT, E.E., and LUESSEN, L.H.: 'Electrical breakdown and discharges in gases' (Plenum Press, 1982), pp. 203–265

31 ROSS, J.N.: 'The diameter of the leader channel using schlieren photography', *Electra*, 1977, (53), pp. 71–73
32 SINGER, H., STEINBIGLER, H., and WEISS, P.: 'A charge simulation method for the calculation of high voltage fields', *IEEE Trans.*, 1974, **PAS-93**, pp. 1660–1668
33 RÜHLING, F., and TRAPP, N.: 'Wideband analog fibre optic data link for high-voltage measurements', *ISH (Athens)*, 1983, paper 64.06
34 FESER, K., and PFAFF, W.: 'A potential-free spherical sensor for the measurement of transient electric fields', *IEEE Trans.*, 1984, **PAS-103**, pp. 2904–2911